



Contents lists available at ScienceDirect

Engineering

journal homepage: [www.elsevier.com/locate/eng](http://www.elsevier.com/locate/eng)

Research  
Green Chemical Engineering—Article

## Designing a Mordenite Catalyst with Enhanced Acidity for Dimethyl Ether Carbonylation by Engineering Open Sn Sites

Ying Li <sup>a,c</sup>, Man Yu <sup>a</sup>, Guodong Qi <sup>b</sup>, Yunduo Liu <sup>a</sup>, Jing Lv <sup>a</sup>, Shouying Huang <sup>a,\*</sup>, Xinbin Ma <sup>a,\*</sup>

<sup>a</sup> Key Laboratory for Green Chemical Technology of Ministry of Education, Collaborative Innovation Center of Chemical Science and Engineering, School of Chemical Engineering and Technology, Tianjin University, Tianjin 300350, China

<sup>b</sup> National Center for Magnetic Resonance in Wuhan & State Key Laboratory of Magnetic Resonance and Atomic and Molecular Physics & Key Laboratory of Magnetic Resonance in Biological Systems, Wuhan Institute of Physics and Mathematics, Innovation Academy for Precision Measurement Science and Technology, Chinese Academy of Sciences, Wuhan 430071, China

<sup>c</sup> Inner Mongolia Key Laboratory of Industrial Catalysis, College of Chemical Engineering, Inner Mongolia University of Technology, Hohhot 010051, China

### ARTICLE INFO

#### Article history:

Received 27 September 2022

Revised 9 December 2022

Accepted 14 January 2023

#### Keywords:

Zeolite  
Sn modification  
Carbonylation  
Brønsted acid catalysis  
Acidic strength

### ABSTRACT

Due to their tunable acidity, shape selectivity, and excellent stability, zeolites are of great importance as solid acid materials in industrial catalysis. Tuning the properties of the acid sites in zeolites allows for the rational design and fabrication of catalysts for target reactions. Dimethyl ether (DME) carbonylation, a critical chain-growth reaction for C1 resource utilization, is selectively catalyzed by the Brønsted acid sites within the eight-membered rings (8-MRs) of mordenite (MOR). It is anticipated that strengthening the Brønsted acidity—particularly in 8-MRs—will improve the catalytic performance of MOR. In this work, density functional theory (DFT) calculations are first employed and the results used to design a modified MOR with stannum (Sn) and to predict the corresponding changes in acidity. Guided by the theoretical studies, a series of Sn-modified MOR are synthesized via a defect-engineering and subsequent heteroatom-substitution strategy. After partial desilication, isolated tetrahedral Sn species in an open configuration are successfully synthesized for the first time, within which tetrahedrally coordinated Al sites are preserved. An acidic characterization is used to confirm that the acidity of the Brønsted acid sites is enhanced by the introduction of the Sn species; as a result, the sample exhibits excellent activity in DME carbonylation reaction. Kinetic and DFT studies reveal that this strengthened acidity facilitates the adsorption of DME and reduces the activation barriers of DME dissociation and acetyl formation, accounting for the improved activity. The work demonstrates mechanistic insights into the promoting effects of strong acidity on DME carbonylation and offers a promising strategy to precisely control the acidic strength of zeolites.

© 2024 THE AUTHORS. Published by Elsevier LTD on behalf of Chinese Academy of Engineering and Higher Education Press Limited Company. This is an open access article under the CC BY-NC-ND license (<http://creativecommons.org/licenses/by-nc-nd/4.0/>).

### 1. Introduction

Zeolites are crystalline aluminosilicate materials that have been widely employed as solid acid catalysts in the chemical industry for processes such as methanol-to-olefin (MTO) reactions [1], fluid catalytic cracking [2], isomerization [3], and alkylation [4], due to their well-defined microporous structure, high thermal stability, and tunable acidity [5]. The bridging hydroxy groups introduced by the substitution of framework tetrahedral Si atoms with trivalent heteroatoms (e.g., Al) result in Brønsted acid sites (BAS) that can transfer protons to reacting substrates. In general, the excep-

tional catalytic properties of zeolite not only depend on the ordered spatial structure but are also strongly governed by the acid characteristics, including the number, strength, accessibility, and proximity to other potential active sites.

The strength of BAS, which is usually assessed using the deprotonation energy (DPE) or adsorption enthalpy ( $\Delta H_{\text{ads}}$ ) of a probe molecule (e.g., ammonia (NH<sub>3</sub>) and pyridine), is responsible for the stability of the adsorbed intermediates and transition states during a reaction [6]. Therefore, it has been regarded as an important descriptor that governs both activity and selectivity in acid catalysis. For example, in the methylation of lower olefins, Arvidsson et al. [7] established a linear scaling relationship between the enthalpies of the transition states and  $\Delta H_{\text{ads}}$  (NH<sub>3</sub>), making it possible to predict reactivity as a function of BAS strength by means of

\* Corresponding authors.

E-mail addresses: [huangsy@tju.edu.cn](mailto:huangsy@tju.edu.cn) (S. Huang), [xbma@tju.edu.cn](mailto:xbma@tju.edu.cn) (X. Ma).

<https://doi.org/10.1016/j.eng.2023.01.020>

2095-8099/© 2024 THE AUTHORS. Published by Elsevier LTD on behalf of Chinese Academy of Engineering and Higher Education Press Limited Company.

This is an open access article under the CC BY-NC-ND license (<http://creativecommons.org/licenses/by-nc-nd/4.0/>).

microkinetic modeling. In methanol dehydration, Jones et al. [8] found that the formation rates of the intermediates (i.e., H-bonded CH<sub>3</sub>OH monomers and protonated dimers) decreased exponentially with the increasing DPE of both the polyoxometalates and MFI zeolite, due to the less stable adsorbed species and transition states. In the MTO process, a higher acid strength facilitates the dissociation of C–O bonds and the formation of C–C bonds. As a result, zeolites with stronger acidity typically exhibit a shorter catalyst lifetime and higher paraffin selectivity in MTO reactions [9].

The carbonylation of dimethyl ether (DME) has been established as a typical Brønsted acid-catalyzed reaction. The product, methyl acetate (MA), is an important industrial feedstock. For example, methyl acrylate and methyl methacrylate can be produced through an aldol condensation between MA and methyl aldehyde [10], and acetic anhydride is produced through the carbonylation of MA [11]. Moreover, MA has been widely used as a solvent in many applications [12,13]. Recently, a promising alternative route to synthesize ethanol, which is commonly used as a transport fuel and gasoline additive, has been proposed via MA hydrogenation [14]. This route has attracted a great deal of attention due to the absence of the ethanol–H<sub>2</sub>O azeotrope, which is an energy-intensive separation process that is inevitably generated during fermentation processes. Thus, DME carbonylation has become a key step in C1 resource (syngas or CO<sub>2</sub>) utilization. Previous studies have demonstrated that zeolites with eight-membered rings (8-MRs; e.g., mordenite (MOR) [15,16], ferrierite (FER) [17], SSZ-13 [18], EU-12 [19], and SUZ-4 [20]) show excellent MA selectivity (>99%), benefiting from spatial confinement of the pore structure. Thus far, most efforts in this direction have focused on tuning the concentration and distribution of BAS in zeolites to improve the activity of DME carbonylation. In comparison, our previous studies have demonstrated that the acid strength of BAS is vital for MA formation [21–23]. However, it remains a significant challenge to strengthen the acidity of BAS while maintaining the number of BAS.

Significant efforts have been devoted to regulating the acidity of aluminosilicate zeolites. One efficient way is to adjust the silicon/aluminum ratio (Si/Al) via desilication and/or dealumination [24,25]. However, the dissolution of framework T sites results in a considerable loss of active sites, as well as partial decay of the ordered structure. Furthermore, new BAS created by means of the isomorphous substitution of framework T atoms with trivalent ions (e.g., Ga<sup>3+</sup>, B<sup>3+</sup>, and Fe<sup>3+</sup>) unfortunately exhibit a decrease in acidity, in most cases [8]. Recently, adjusting the spatial proximity/interaction between the BAS and Lewis acid sites has proven successful in increasing the acid strength [26–28]. Heteroatoms (e.g., stannum (Sn) or zirconium (Zr)) that are introduced into zeolites can function as electron-withdrawing groups [29–31], which inspired us to improve the acidic strength of MOR zeolite using this approach.

In this research, we fabricated a series of Sn-modified MORs via a defect-engineering and subsequent heteroatom-substitution strategy, by which tetrahedral Sn sites with spatial proximity/interaction with the BAS were successfully introduced. More importantly, the framework Si atoms—rather than the framework Al atoms—were replaced by Sn for the first time, allowing tetrahedrally coordinated Al sites to be well preserved. This approach is particularly applicable to Brønsted acid-catalyzed reactions. The crucial roles of closed Sn sites ((SiO)<sub>4</sub>–Sn) and open Sn sites ((HO)–Sn–(OSi)<sub>3</sub>) on Brønsted acidity were established through density functional theory (DFT) calculations, where the latter was shown to be more efficient in improving the acidity. The acidic strength of BAS in the 8-MRs was then experimentally investigated and showed both qualitative and quantitative agreement with the DFT results. The contribution of this acidity to catalysis was

demonstrated in the carbonylation of DME as a representative application. Finally, DFT calculations, kinetic analysis, and *in situ* experiments were combined to provide mechanistic insights into the promoting effects of enhanced Brønsted acidity.

## 2. Experimental section

### 2.1. Catalyst preparation

The parent zeolite was a sodium (Na)-form MOR sample, which was purchased from Yangzhou Zhonghe Petroleum Chemicals Institute Co., Ltd. (China), labeled as Si/Al = 10. The sample was ion-exchanged twice with 0.2 mol·L<sup>-1</sup> NH<sub>4</sub>NO<sub>3</sub> solution. After being dried at 110 °C and calcinated at 500 °C, the H-form MOR sample (labeled as HM) was obtained.

Sn-modified MOR zeolites were prepared via a two-step post-treatment, which consisted of desilication and the introduction of Sn species. In brief, commercial Na-MOR was treated in 0.2 mol·L<sup>-1</sup> ammonia solution (25 mL per gram of zeolite) at 65 °C for 30 min. After filtration, washing, and drying, the as-prepared sample was converted to HM via ion exchange with NH<sub>4</sub>NO<sub>3</sub> solution. The obtained powder was finely ground with the designed amount of (CH<sub>3</sub>)<sub>2</sub>SnCl<sub>2</sub> in a glovebox, and then transferred into a tubular reactor. The xSn-AM samples (where x is the actual mass fraction of Sn measured using inductively coupled plasma–optical emission spectrometry (ICP-OES), and AM stands for alkaline-treated MOR) were obtained after calcination at 500 °C for 6 h in nitrogen (N<sub>2</sub>) and subsequent air calcination for 5 h. The preparation process is diagrammatically represented in Fig. S1 (Appendix A). In addition, a sample without Sn species was prepared as a reference, labeled as AM; the procedure included the above steps for preparing xSn-AM but without the addition of (CH<sub>3</sub>)<sub>2</sub>SnCl<sub>2</sub>.

For comparison, we prepared two Sn-containing samples using different methods (Fig. S1). The ySnO<sub>2</sub>/HM was obtained by milling HM and SnO<sub>2</sub> mixture. To illustrate the significance of desilication on Sn incorporation, HM was mixed with (CH<sub>3</sub>)<sub>2</sub>SnCl<sub>2</sub> directly in a glovebox. The subsequent calcination was similar to that of xSn-AM. The prepared sample was denoted as zSn-HM. Here, y and z refer to the actual mass fractions of Sn in ySnO<sub>2</sub>/HM and zSn-HM samples, respectively.

All the Na-form samples used in the deuterated acetonitrile (CD<sub>3</sub>CN) adsorption experiment were prepared through steps similar to those used for AM and xSn-AM, but the Na-form MOR was used as the parent when conducting the subsequent ammonia treatment and dry impregnation.

### 2.2. Characterization

ICP-OES was performed on a Varian VISTA MPX (Varian, USA) to determine the actual content of Si, Al, and Sn in the samples. Diffuse reflectance ultraviolet–visible (UV-Vis) spectra were acquired on a Hitachi U-3010 (Hitachi Ltd., Japan) spectrophotometer against BaSO<sub>4</sub>. The samples were dehydrated in N<sub>2</sub> at 450 °C prior to spectra collection. X-ray photoelectron spectroscopy (XPS) experiments were conducted on a PerkinElmer PHI 1600 ESCA system (PerkinElmer, USA) with Al Kα (E = 1486.6 eV) radiation. C 1s at 284.6 eV was used as a reference for the binding energy calibration.

NH<sub>3</sub> temperature-programmed desorption (TPD) was carried out on a Micromeritics AutoChem II 2920 instrument (Micromeritics Instrument Corporation, USA). In a typical run, 100 mg of sample was placed into a quartz U-tube and dehydrated in an argon (Ar) atmosphere at 450 °C for 1 h. Subsequently, a 10% NH<sub>3</sub>/helium (He) mixture was admitted into the tube at 200 °C for 1 h, and then

the sample was flushed with He for 1 h to remove the gaseous and weakly adsorbed NH<sub>3</sub>. Finally, the released NH<sub>3</sub> was detected using a thermal conductivity detector (TCD) from 150 to 850 °C with a ramp rate of 10 °C·min<sup>-1</sup>.

<sup>1</sup>H-<sup>13</sup>C cross-polarization (CP)/magic-angle spinning (MAS) nuclear magnetic resonance (NMR) spectra were recorded at 11.7 T on a Bruker Avance III spectrometer (Bruker, Germany). The resonance frequencies were 500.58 and 125.89 MHz for <sup>1</sup>H and <sup>13</sup>C, respectively. Prior to each run, 0.15 g of sample was loaded into a glass tube and evacuated under a vacuum of 10<sup>-3</sup> Pa at 400 °C for 16 h. To solely determine the acidity of BAS in the 8-MRs, pyridine titration was employed to selectively shield the acid sites in the 12-membered rings (12-MRs). More specifically, excess pyridine-*d*<sub>5</sub> vapor was introduced into the tube after the sample was cooled to room temperature. Then, the tube was sealed and heated at 200 °C for 2 h, followed by degassing for 2 h to remove physisorbed pyridine-*d*<sub>5</sub>. Subsequently, about 0.5 mmol·g<sup>-1</sup> 2-<sup>13</sup>C-acetone was introduced. Finally, the sample was transferred into a zirconia NMR rotor in a glovebox.

All Fourier-transform infrared (FTIR) spectra were collected on a Nicolet 6700 spectrometer (Thermo Electron Scientific Instruments Corporation, USA) equipped with a mercury cadmium telluride detector, by averaging 32 scans. The resolution was set as 4 cm<sup>-1</sup>. Zeolite samples (~15 mg) were pressed into self-supporting wafers with a diameter of 1.3 cm and placed into a stainless-steel cell with CaF<sub>2</sub> windows (the QIRS-A02 *in situ* quartz cell from Tuozheng Company (China)). Prior to each experiment, the sample was *in situ* evacuated at 450 °C for 1 h. After the sample was cooled to 150 °C, the background spectrum was collected. The adsorptions of CD<sub>3</sub>CN and pyridine were used to determine the configuration of the Sn species and quantify the amount of BAS in the 12-MRs, respectively. After saturation with CD<sub>3</sub>CN vapor at 30 °C, the samples were outgassed and heated to 150 °C to remove the gaseous and physically adsorbed species. The infrared (IR) spectra of the CD<sub>3</sub>CN adsorption were recorded at 150 °C after degassing for 10 min. For pyridine adsorption, the catalysts were saturated with pyridine at 150 °C for 30 min, followed by evacuating for 30 min.

The acidic strength of the BAS in the 8-MRs was exclusively analyzed based on the NH<sub>3</sub>-IR-TPD of pyridine-saturated MOR. After the pyridine adsorption experiment, the samples were exposed to 10% NH<sub>3</sub>/He for 30 min, and then degassed for 30 min. Subsequently, IR spectra were obtained *in vacuo* every 2 °C from 150 to 550 °C at the desired temperature ramp rate (5, 10, 15, and 20 °C·min<sup>-1</sup>). Here, a differential change in the absorbance of the IR band at 1427 cm<sup>-1</sup> related to NH<sub>3</sub> bonding with BAS (i.e., -d(I<sub>1427</sub>)/dT) reflects the desorption rate of NH<sub>3</sub>.

Experiments on the temperature-programmed surface reaction (TPSR) were conducted on a flow microreactor connected to a quadrupole mass spectrometer (Hiden HPR-20, Hiden Analytical, USA). Prior to measurements, approximately 150 mg of sample was put into the reactor and then treated at 450 °C for 1 h. After the sample was cooled to 200 °C, a flow of 5% DME/He (10 mL·min<sup>-1</sup>) was switched in. The signals of the DME (*m/e*=45) and methanol (*m/e*=32) were recorded for 30 min. After He purging for 30 min, carbon monoxide (CO) was introduced into the reactor, followed by He flushing for an additional 30 min. Then, the MA formation rate was measured based on the signal of *m/e*=43 during exposure to the DME stream (10 mL·min<sup>-1</sup>).

The acetyl formation rate was measured via an *in situ* FTIR experiment. In a typical run, the self-supporting wafer (~15 mg) was heated at 450 °C in flowing He for 1 h and then cooled to 200 °C. After 30 min of exposure to the DME gas, the stream was switched to He to clean the surface. Then, the background spectrum was acquired. Subsequently, CO gas was introduced into the cell and IR spectra were collected every 20 s.

### 2.3. Catalytic evaluation

The catalysts were evaluated in a fixed-bed reactor. In each run, 1 mL of catalyst in 40–60 mesh (~0.5 g) was pretreated in N<sub>2</sub> at 200 °C. Then, the gaseous reactant mixture (the volume ratio of DME and CO *V*<sub>DME</sub>:*V*<sub>CO</sub>=2:98) was introduced into the reactor with a gas hourly space velocity (GHSV) of 6000 h<sup>-1</sup>. During the reaction, the pressure was maintained at 1.5 MPa. The reaction outlet was analyzed online using a gas chromatograph (Shimadzu GC-2014C, Shimadzu, Japan). Organic components such as DME, MA, and hydrocarbons (e.g., CH<sub>4</sub> and C<sub>2</sub>H<sub>4</sub>) were separated by means of a PLOT Q column and analyzed using a flame ionization detector (FID). CO and N<sub>2</sub> were separated by means of two Porapak N and one MS-13X column and analyzed using a TCD. The conversion of DME (*X*<sub>DME</sub>), selectivity to MA (*S*<sub>MA</sub>), space-time yield of MA (STY<sub>MA</sub>), and turnover frequency (TOF) were calculated using equations reported previously [32] (Eqs. (1)–(4)).

$$X_{\text{DME}} = \frac{n_{\text{DME},i} - n_{\text{DME},o}}{n_{\text{DME},i}} \times 100\% \quad (1)$$

$$S_{\text{MA}} = \frac{3n_{\text{MA}}}{\sum n_i N_i} \times 100\% \quad (2)$$

where *n*<sub>DME,i</sub> and *n*<sub>DME,o</sub> are the mole number (mol) of DME at the inlet and outlet, respectively; *n*<sub>MA</sub> is mole number (mol) of MA at the outlet; *n*<sub>*i*</sub> is the mole number (mol) of component *i* at the outlet; and *N*<sub>*i*</sub> is the number of CH<sub>3</sub> groups in the product *i* at the outlet.

$$\text{STY}_{\text{MA}} = \frac{\dot{n}_{\text{DME}} \times X_{\text{DME}} \times S_{\text{MA}} \times 74}{m_{\text{cat}}} \quad (3)$$

$$\text{TOF} = \frac{\dot{n}_{\text{DME}} \times X_{\text{DME}}}{m_{\text{cat}} \times 1000 \times N_{\text{BAS}}} \quad (4)$$

where STY<sub>MA</sub> is the space-time yield (g·kg<sup>-1</sup>·h<sup>-1</sup>) of MA, TOF is the turnover frequency (h<sup>-1</sup>), *n*<sub>DME</sub> is the total molar flow rate (mol·h<sup>-1</sup>) of DME, 74 (g·mol<sup>-1</sup>) is the molar mass of MA, *m*<sub>cat</sub> (kg) is the mass of catalyst, *N*<sub>BAS</sub> is the number (mol·g<sup>-1</sup>) of BAS in 8-MRs.

### 2.4. Computational details

All DFT calculations were carried out using the DMol<sup>3</sup> program package in Materials Studio (Accelrys, USA). The functional and electronic setup were consistent with our previous study [32]. Moreover, the Ortmann–Bechstedt–Schmidt (OBS) method was used to describe the dispersion correction between molecules and the zeolite framework. The convergence criteria were set to 2 × 10<sup>-5</sup> hartree (1 hartree = 2625.5 kJ·mol<sup>-1</sup>) for energy, 4 × 10<sup>-3</sup> hartree·Å<sup>-1</sup> for maximum force, and 5 × 10<sup>-3</sup> Å for maximum displacement. To verify the reliability of the results, we improved the convergence criteria to calculate the DPE values and adsorption energies of NH<sub>3</sub> on BAS. The results listed in Table S1 (Appendix A) demonstrate that improving the convergence criteria had little influence on the DFT results. The reaction transition states were searched by means of complete linear synchronous transit/quadratic synchronous transit and confirmed by calculating the vibrational frequencies.

Cluster models of MOR were derived from the periodic MOR structure. MOR has four distinct tetrahedral sites (labeled as T1, T2, T3, and T4). Among them, the T2 and T4 sites are located in the 12-MRs, the T3 site is in the 8-MRs, and the T1 site is shared by the two channels (Fig. S2 in Appendix A). Since T3-O33 in the 8-MRs has been shown to be as the active site for DME carbonylation, one Si atom at the T3 site was replaced by an Al atom. Meanwhile, the negative charge was compensated for by a proton linked to the O33 site. A cluster model with 44 tetrahedra enclosing the

8-MR side pocket at the center of the structure was built to explore the effect of tetrahedrally coordinated Sn species on the acidity of the T3-O33 site and to calculate the activation energies of elementary reactions in DME carbonylation (shown in Figs. S3(a)–(c) in Appendix A). As shown in Fig. S3(d) (Appendix A), all the tetrahedral Si sites in the 8-MRs were considered as possible locations for Sn substitution. These sites were denoted as T-locations. For example, the T3 located in the lower right of the 8-MR was denoted as T3-LR. In order to maintain the zeolite structure, these tetrahedral sites, together with their four linked  $-\text{O}-(\text{SiO})_4-$  groups, were allowed to relax while all the other atoms were fixed. All the dangling bonds were saturated with H atoms at 1.11 Å from the O atoms and orientated toward the position of the Si atoms in the next coordination sphere.

The DPE corresponds to the energy required to cleave a H atom from a framework O atom in zeolite. The DPE was calculated as shown in Eq. (5).

$$\text{DPE} = E_{\text{MOR}^-} - E_{\text{MOR}} \quad (5)$$

where  $E_{\text{MOR}^-}$  is the energy of the zeolite framework anion and  $E_{\text{MOR}}$  is the energy of the optimized zeolite. A smaller DPE indicates stronger acidity.

The adsorption energies of the adsorbates ( $E_{\text{ads-adsorbate}}$ ) were defined as shown in Eq. (6).

$$E_{\text{ads-adsorbate}} = E_{\text{adsorbate-MOR}} - E_{\text{adsorbate}} - E_{\text{MOR}} \quad (6)$$

where  $E_{\text{adsorbate-MOR}}$  and  $E_{\text{adsorbate}}$  are the energies of the optimized zeolite with adsorbates and the isolated molecule of the adsorbates, respectively. A more negative  $E_{\text{adsorbate-DFT}}$  corresponds to a more stable adsorption.

The activation energies ( $E_{\text{act}}$ ) and reaction energies ( $\Delta E$ ) of the elementary steps were calculated as shown in Eqs. (7) and (8), respectively.

$$E_{\text{act}} = E_{\text{TS}} - E_{\text{reactant-Z}} \quad (7)$$

$$\Delta E = E_{\text{product-Z}} - E_{\text{reactant-Z}} \quad (8)$$

where  $E_{\text{TS}}$ ,  $E_{\text{reactant-Z}}$ , and  $E_{\text{product-Z}}$  are respectively the energies of the transition state, reactant, and product.

### 3. Results and discussion

#### 3.1. Theoretical calculations toward Brønsted acidity in Sn-modified MOR

According to previous theoretical and experimental studies [21–23], the acidity of BAS governs the catalytic performance of zeolite in DME carbonylation. Given that the Brønsted acid at the T3-O33 site in MOR is recognized as the active site [15], we first investigated the influence of Sn modification on the nature of this site using DFT calculations. The heteroatom Sn can be tetrahedrally coordinated to the zeolitic framework in two configurations [33,34]: closed (Figs. 1(a)–(c)) and open (Figs. 1(d)–(f)) Sn sites. The DPE and adsorption energy of  $\text{NH}_3$  ( $E_{\text{ads-NH}_3}$ ) of these configurations were calculated to evaluate the acidic strength. All the tetrahedral Si sites in the 8-MRs were considered as possible locations for Sn substitution (Fig. 1(g)). As listed in Table 1, all the DPE and adsorption energy of  $\text{NH}_3$  values of H-[Al,Sn]-MOR are lower than those of H-[Al]-MOR, except for the Sn at the T3-upper right (UR) site. This finding indicates that the Brønsted acidity at T3-O33 site can be enhanced by both open and closed Sn sites in MOR, in line with our hypothesis. Furthermore, open Sn species result in stronger Brønsted acidity when the Sn atom is located at the same T site. Considering that stronger acid strength can efficiently lower the activation barrier of acetyl formation [22,23], we

chose MOR with open Sn species—that is, exhibiting enhanced Brønsted acidity—as the target to fabricate for DME carbonylation.

#### 3.2. Fabrication of MOR with open Sn species

Guided by the DFT results, we aimed to engineer MOR with open Sn sites. A two-step post-synthetic strategy has been proposed to synthesize metal-isomorphous substituted zeolite [30,35]. After partial removal of framework T atoms, heteroatom species (e.g., Sn, Zn) can be successfully introduced into the created defects. Dealumination using an acidic solution has been commonly used to create defects in previous reports [35,36]. However, for DME carbonylation, the active sites are BAS formed by the charge-balance of the framework  $[\text{AlO}_4]^-$ . Therefore, it is a prerequisite to preserve the tetrahedrally coordinated Al as much as possible when additional Sn sites are introduced. Herein, treatment in a diluted alkaline solution (i.e., ammonia) was employed to achieve partial desilication. Subsequently, Sn sites were grafted onto the Si vacancies by means of dry impregnation. The textural properties and element compositions of the as-prepared xSn-AM catalysts were investigated using X-ray diffraction (XRD), ICP-OES,  $\text{N}_2$  physisorption, and scanning electron microscope (SEM) measurements.

The actual amounts of Sn listed in Table 2 confirm that Sn species were introduced into the MOR. The Sn loading of the physically mixed sample (i.e.,  $0.17\text{SnO}_2/\text{HM}$ ) is equal to that of 0.17Sn-AM, which is beneficial for distinguishing the effects of different Sn species on the physicochemical and catalytic properties of MOR. Upon treatment with ammonia solution, the Si content of MOR decreased from 11.130 to 10.818  $\text{mmol}\cdot\text{g}^{-1}$ , while the amount of Al remained unchanged, indicating that the extraction of framework Si species was achieved while the Al sites remained intact. It should be noted that the introduction of Sn was accompanied by a decrease in the amounts of both Si and Al, likely due to the release of gas-phase  $\text{SiCl}_4$  and  $\text{AlCl}_3$  formed by reactions of HCl (a decomposition product of  $(\text{CH}_3)_2\text{SnCl}_2$ ) with framework Si and Al atoms. The diffraction features in the XRD patterns (Fig. S4 in Appendix A, Joint Committee on Powder Diffraction Standards (JCPDS) 43-0171) and typical  $\text{N}_2$  Type I adsorption-desorption isotherms (Fig. S5 in Appendix A) indicate the well-preserved MOR structure of all samples after the two-step post-synthetic treatment. The absence of XRD peaks due to bulk  $\text{SnO}_2$  ( $2\theta = 26.6^\circ$ ,  $33.9^\circ$ , and  $37.9^\circ$ ) demonstrates that the Sn species were highly dispersed in the MOR. The textural parameters (Table 2) and representative SEM images (Fig. S6 in Appendix A) show negligible variations in terms of the pore structure and particle size for all samples. These observations provide a solid foundation for solely investigating the nature and role of Sn species in DME carbonylation.

The nature of the Sn species in xSn-AM was explored by means of UV-Vis and XPS spectroscopy. As shown in Fig. 2(a), both pure and alkaline-treated MOR (HM and AM) exhibit an intense band centered at 218 nm, which is related to the aluminosilicate matrix [37]. This band shifts to 222 nm after the isomorphous substitution of Sn via the two-step procedure, due to the charge transition from  $\text{O}^{2-}$  to tetrahedrally coordinated  $\text{Sn}^{4+}$  species [38,39]. The Sn 3d XPS spectra of 0.17Sn-AM and 0.28Sn-AM, which exhibit a low signal-to-noise ratio and poor peak definition (Fig. 2(b)), show two peaks at 487.5 and 497.3 eV. These peaks are attributable to the  $3d_{5/2}$  and  $3d_{3/2}$  photoelectrons of the tetrahedral framework Sn [40]. For the physically mixed sample ( $0.17\text{SnO}_2/\text{HM}$ ), a shoulder peak at 280 nm emerges, indicating the presence of  $\text{SnO}_2$  species. This is also evidenced by the two characteristic signals of  $\text{SnO}_2$  (i.e., 486.8 and 495.6 eV) in the XPS spectrum [41]. To demonstrate the necessity of pre-alkaline treatment in the preparation procedure, we calcinated a mixture of  $(\text{CH}_3)_2\text{SnCl}_2$  and untreated

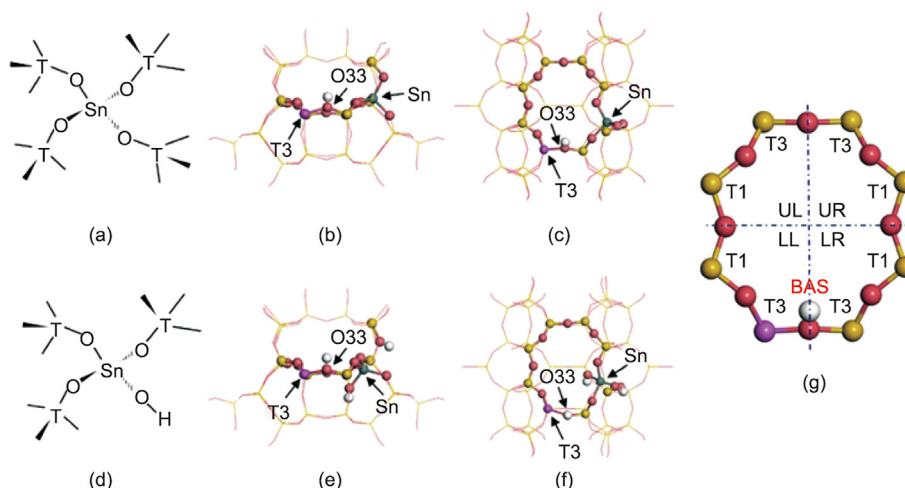


**Fig. 1.** (a–f) Schematic of tetrahedrally coordinated Sn species in zeolite: (a) diagram, (b) front, and (c) top view of the closed Sn site; (d) diagram, (e) front, and (f) top view of the open Sn site. (g) Labels of the considered T sites for Sn substitution. UL: upper left; UR: upper right; LL: lower left; LR: lower right. Atoms are labeled as follows: purple: Al; yellow: Si; pink: O; grey: Sn; white: H.

**Table 1**

Calculated values of DPE and adsorption energy of  $\text{NH}_3$  on BAS at the T3-O33 site in H-[Al]-MOR and H-[Al,Sn]-MOR.

Catalyst	Location of Sn	Closed Sn		Open Sn	
		DPE ( $\text{kJ}\cdot\text{mol}^{-1}$ )	$E_{\text{ads-NH}_3}$ ( $\text{kJ}\cdot\text{mol}^{-1}$ )	DPE ( $\text{kJ}\cdot\text{mol}^{-1}$ )	$E_{\text{ads-NH}_3}$ ( $\text{kJ}\cdot\text{mol}^{-1}$ )
H-[Al]-MOR	—	1311	−166	1311	−166
H-[Al,Sn]-MOR	T3-LR	1335	−155	— <sup>a</sup>	— <sup>a</sup>
	T1-LR	1298	−183	1298	−183
	T1-UR	1303	−174	1299	−176
	T3-UR	1309	−165	1304	−169
	T3-UL	1309	−166	1302	−169
	T1-UL	1297	−168	1295	−183
	T1-LL	1304	−165	1283	−183

<sup>a</sup> BAS at T3-O33 will be destroyed in this case.

**Table 2**

Summary of the chemical compositions and textural properties of the MOR catalysts.

Sample	Element content ( $\text{mmol}\cdot\text{g}^{-1}$ )			Sn loading (wt%)	Si/Al	$S_{\text{total}}$ ( $\text{m}^2\cdot\text{g}^{-1}$ )	Total pore volume ( $\text{cm}^3\cdot\text{g}^{-1}$ )
	Si	Al	Sn				
HM	11.130 ± 0.062	1.242 ± 0.024	0	0	9.0	532	0.21
AM	10.818 ± 0.057	1.234 ± 0.019	0	0	8.8	525	0.22
0.1Sn-AM	10.134 ± 0.059	1.178 ± 0.015	0.008	0.096	8.6	524	0.22
0.17Sn-AM	10.069 ± 0.083	1.176 ± 0.020	0.014	0.167	8.6	516	0.21
0.28Sn-AM	9.749 ± 0.061	1.158 ± 0.017	0.023	0.279	8.4	529	0.22
0.17SnO <sub>2</sub> /HM	10.078 ± 0.087	1.116 ± 0.030	0.014	0.167	9.0	530	0.21

HM—that is, 0.17Sn-HM. The almost identical UV-Vis and XPS features of 0.17Sn-HM in comparison with 0.17SnO<sub>2</sub>/HM suggest that framework T vacancies are essential for incorporating Sn into the tetrahedral coordinated environment.

<sup>29</sup>Si MAS NMR was also performed to shed some light on the coordination environment of the Si atoms. As shown in Fig. 3(a), the <sup>29</sup>Si MAS NMR spectra of HM, AM, and 0.17Sn-AM display two peaks with shoulders between −90 and −120 ppm. The peak between −110 and −115 ppm is attributable to the Q4 [Si(SiO)<sub>4</sub>] site, and the peak at around −103.4 ppm is assigned to the Q3 [Si(SiO)<sub>3</sub>M]. After the alkaline treatment, the peak of the Q3 site in AM was broadened by the rising shoulder at around −102 ppm. To determine the accurate chemical shift of the shoulder, we deconvoluted the spectra by fixing the peak of Q3 [Si(SiO)<sub>3</sub>M] at −103.4 ppm (Fig. S7 in Appendix A). It was found that a small peak at −102.8 ppm arose, which is attributed to the [Si(SiO)<sub>3</sub>OH] units [42]. This evidences the formation of framework defects.

Further dry impregnation of Sn onto AM led to a narrower peak of the Q3 site in 0.17Sn-AM, indicating the reduction of [Si(SiO)<sub>3</sub>OH] units. This observation also confirms that Sn atoms have been successfully incorporated into the vacancies of MOR through the employed two-step post-synthetic strategy.

To further determine the configuration of the tetrahedrally coordinated Sn species, CD<sub>3</sub>CN was employed as a probe molecule. In CD<sub>3</sub>CN-adsorption IR experiments, the vibration of the C≡N bond will be perturbed by the open Sn sites to 2316 cm<sup>−1</sup> or by the closed Sn sites to 2308 cm<sup>−1</sup>, from 2265 cm<sup>−1</sup> in gaseous CD<sub>3</sub>CN [33,43]. Since the interaction between CD<sub>3</sub>CN and BAS also gives rise to IR characteristics around 2200–2350 cm<sup>−1</sup> [44,45], we conducted CD<sub>3</sub>CN adsorption over completely Na<sup>+</sup>-exchanged samples to eliminate the peak overlapping associated with Sn (regardless of open or closed sites) and BAS. Fig. 3(b) presents the normalized spectra. As expected, a strong band at 2279 cm<sup>−1</sup> appears over all Na-form samples, which can be considered to be a feature

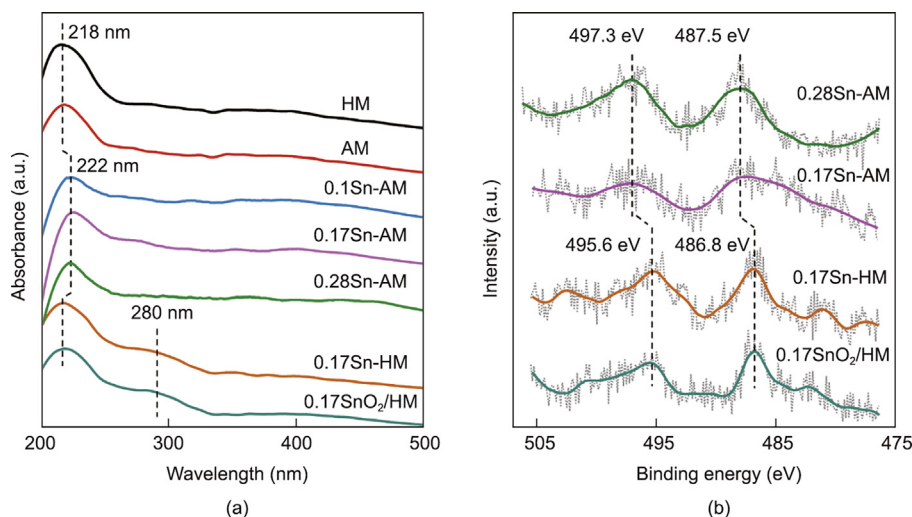


Fig. 2. (a) UV-Vis and (b) Sn 3d XPS spectra of samples.

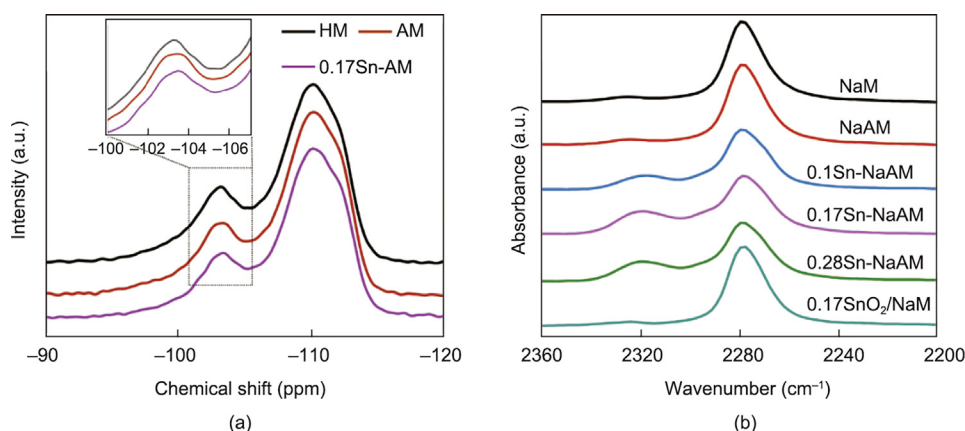


Fig. 3. (a)  $^{29}\text{Si}$  MAS NMR spectra of samples; (b) the IR spectra of  $\text{CD}_3\text{CN}$  adsorbed on Na-form samples.

of the interaction between  $\text{CD}_3\text{CN}$  and  $\text{Na}^+$  in zeolites [46]. Meanwhile, a weak band caused by the open Sn sites ( $2316\text{ cm}^{-1}$ ) can be observed over the Sn-incorporated samples, whose intensity increases as the Sn content increases (0, 0.1%, and 0.17%). As the Sn content increases further, the peak intensity no longer increases, because of the limited framework T defects. To discriminate among the open and closed sites, the IR spectra of  $\text{CD}_3\text{CN}$  adsorption were deconvoluted. However, even when we fixed the peak position at  $2308\text{ cm}^{-1}$ , this peak went back to baseline after fitting (red dotted line in Fig. S8 in Appendix A). This result demonstrates that most of the Sn atoms exist in open configurations in xSn-AM. Moreover, even if just a few closed Sn sites are present in the samples, they would be converted to open sites by the water generated in the induction period of the DME carbonylation reaction [47,48]. Based on the above characterization, it can be confirmed that Sn-substituted MOR with open Sn sites was successfully prepared via the two-step post-synthetic procedure.

### 3.3. Acidic properties

Since BAS function as the active centers for DME carbonylation, assessing the acidic properties (including concentration, distribution, and strength) of the Sn-modified MOR catalysts is of great significance. The total amount of BAS ( $B_{\text{total}}$ ) was determined by means of  $\text{NH}_3$ -TPD measurements (Fig. 4(a)).  $\text{NH}_3$  molecules,

which have a small diameter (0.26 nm), are able to access the BAS in both the 8-MRs and 12-MRs. Each  $\text{NH}_3$ -TPD profile was decomposed into three peaks centered at about 230, 330, and  $570\text{ }^\circ\text{C}$ , respectively. According to previous studies [32,49], the first two peaks are caused by weak and moderate acid sites, while the third is mainly contributed by the BAS. We calculated the  $B_{\text{total}}$  based on the integral peak areas of  $\text{NH}_3$  desorption. In addition,  $^{27}\text{Al}$  MAS NMR (Fig. S9 in Appendix A) and ICP-OES were combined to determine the number of framework Al ( $\text{Al}_F$ ). As summarized in Table 3, the  $B_{\text{total}}$  for all samples is consistent with the  $\text{Al}_F$ , confirming the reliability of the acid quantification. Compared with the parent AM and HM, a decrease in BAS was observed over xSn-AM, reconfirming that a slight abstraction of framework T atoms occurred during the dry impregnation of Sn by the  $(\text{CH}_3)_2\text{SnCl}_2$  precursor. Notably, the  $B_{\text{total}}$  of  $0.17\text{SnO}_2/\text{HM}$  is almost equal to that of HM. This finding suggests that introducing  $\text{SnO}_2$  by physical mixing has a very limited impact on the Brønsted acidity of MOR. Unlike  $\text{NH}_3$ , pyridine—as another basic probe molecule—can selectively detect the BAS in the 12-MRs due to its large diameter (5.4 nm) [16,32]. Thus, the number of BAS in the 12-MRs ( $B_{12\text{-MR}}$ ) was quantified by means of the IR spectra of pyridine adsorption (Fig. 4(b)). The peaks at  $1630$  and  $1540\text{ cm}^{-1}$  are assigned to pyridinium ions on BAS, and the bands at  $1450$  and  $1610\text{ cm}^{-1}$  are related to pyridine interacting with the Lewis acid sites. As listed in Table 3, the number of BAS in the 8-MRs ( $B_{8\text{-MR}}$ ) and  $B_{12\text{-MR}}$  of

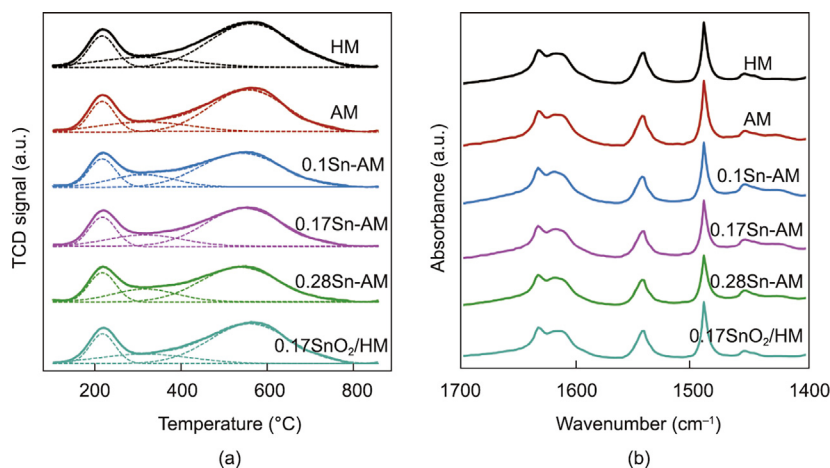


Fig. 4. (a)  $\text{NH}_3$ -TPD profiles and (b) IR spectra of the pyridine adsorption of the MOR catalysts.

Table 3

The quantity of  $\text{Al}_F$  and the BAS of samples ( $\mu\text{mol}\cdot\text{g}^{-1}$ ).

Sample	$\text{Al}_F^a$	$B_{\text{total}}^b$	$B_{12\text{-MR}}^c$	$B_{8\text{-MR}}^d$
HM	954	934	458	475
AM	933	916	443	473
0.1Sn-AM	867	844	389	455
0.17Sn-AM	856	824	385	439
0.28Sn-AM	839	802	376	426
0.17SnO <sub>2</sub> /HM	960	923	427	496

<sup>a</sup>  $\text{Al}_F = \text{Al}_{\text{total}} \times \text{Al}_F\%$ , where  $\text{Al}_{\text{total}}$  and  $\text{Al}_F\%$  were determined via ICP-OES and  $^{27}\text{Al}$  MAS NMR, respectively.

<sup>b</sup> Calculated based on  $\text{NH}_3$ -TPD.

<sup>c</sup> Calculated based on the integral band at  $1540\text{ cm}^{-1}$  and the extinction coefficient of  $1.67\text{ cm}^2\cdot\mu\text{mol}^{-1}$  [50].

<sup>d</sup>  $B_{8\text{-MR}} = B_{\text{total}} - B_{12\text{-MR}}$ .

the xSn-AM samples exhibit similar variations, indicating the indiscriminate removal of framework Al from both channels. Thus, the Sn incorporation does not affect the distribution of BAS.

$^{13}\text{C}$  CP/MAS NMR using 2- $^{13}\text{C}$ -acetone as the probe molecule is a well-established method for detecting the Brønsted acidity of solid acids [27,51]. To exclusively evaluate the strength of BAS within the 8-MRs, we selectively titrated the BAS in the 12-MRs by pyridine- $d_5$  before collecting the NMR spectra. The NMR spectrum of 2- $^{13}\text{C}$ -acetone adsorbed on pyridine-saturated AM exhibits four overlapped peaks (Fig. 5). The signal at 213 ppm is assigned to the

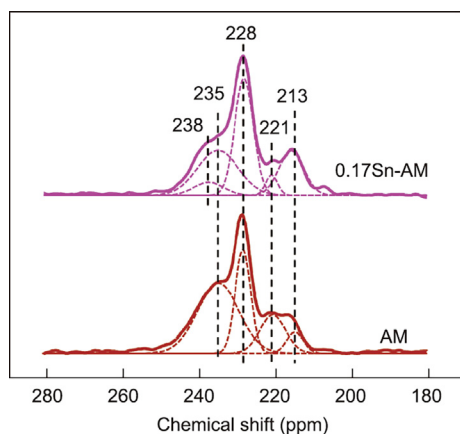


Fig. 5.  $^{13}\text{C}$  CP/MAS NMR spectra of 2- $^{13}\text{C}$ -acetone adsorbed on pyridine-saturated AM and 0.17Sn-AM catalysts.

physically adsorbed 2- $^{13}\text{C}$ -acetone or the acetone dimer [52]. The weak peak at 221 ppm is due to a small amount of unperturbed BAS in the 12-MRs, whose intensity is much stronger in the AM samples without pre-adsorbed pyridine- $d_5$  (Fig. S10 in Appendix A). This result is caused by the incomplete titration of BAS in the 12-MRs or the exchange between the adsorbed pyridine and acetone. The sharp resonance at 228 ppm and the shoulder at 235 ppm are associated with the acetone adsorbed on BAS and the stronger BAS in the 8-MRs [26,53], respectively. For the 0.17Sn-AM catalyst, an additional peak at 238 ppm is clearly resolved in the spectrum, which suggests that the open Sn sites result in remarkably strengthened Brønsted acidity.

To quantitatively assess the strength of the BAS in the 8-MRs, we conducted  $\text{NH}_3$ -IR-TPD experiments on pyridine-saturated MOR. As the BAS in the 12-MRs have been poisoned by pyridine, only the BAS in the 8-MRs can interact with  $\text{NH}_3$ , inducing an IR band at  $1427\text{ cm}^{-1}$  (Figs. 6(a) and (b)). The temperature at the maximum desorption rate ( $T_m$ ) can be determined by differentiating the peak intensity with respect to the temperature (Fig. 6(c)). By varying the heating rate, we calculated the desorption energy of  $\text{NH}_3$  ( $E_{\text{des}}$ ) according to the following equation [54]:

$$\ln\left(\frac{\beta}{T_m^2}\right) = -\frac{E_{\text{des}}}{RT_m} + \ln\left(\frac{E_{\text{des}}A}{RC}\right) \quad (9)$$

where  $\beta$  is the ramp rate, and  $A$  is the number of adsorbed  $\text{NH}_3$  at saturation.  $R$  and  $C$  are the gas constant and the constant related to the rate of desorption, respectively. Fig. 6(d) shows clear linear correlations between  $2\ln T_m - \ln \beta$  and  $1/T_m$  for the AM and xSn-AM samples. The calculated  $E_{\text{des}}$  are 105, 115, 124, and 121  $\text{kJ}\cdot\text{mol}^{-1}$ , respectively. It is clear that the samples with open Sn sites exhibit higher  $E_{\text{des}}$ , which increase with increasing Sn content. Moreover, 0.17Sn-HM exhibits an identical temperature to AM at the maximum  $\text{NH}_3$  desorption rate. This excludes the promotion effect of unincorporated Sn species on acid strength (Fig. S11 in Appendix A). It can be noted from Table 4 that the  $E_{\text{des}}$  changes accordantly with the band intensity at approximately  $2316\text{ cm}^{-1}$  in the  $\text{CD}_3\text{CN}$ -adsorption IR spectra. This finding confirms that the open Sn sites enhance the acidic strength of the BAS in the 8-MRs, which is also in line with the results predicted by the DFT calculations.

#### 3.4. Improved catalytic performance of the Sn-modified catalysts

The catalytic performance, including the conversion of DME ( $X_{\text{DME}}$ ), space-time yield of MA ( $\text{STY}_{\text{MA}}$ ), and selectivity to MA

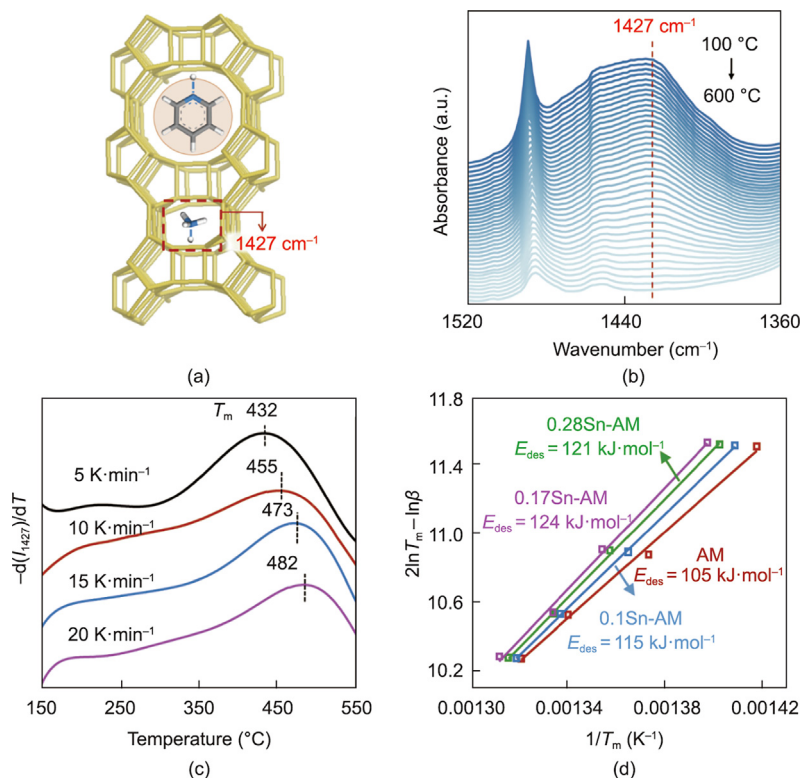


**Fig. 6.** (a) Illustration of the  $\text{NH}_3$ -IR-TPD experiments; (b)  $\text{NH}_3$ -IR-TPD on alkaline-treated MOR (AM); (c)  $\text{NH}_3$ -IR-TPD at different ramps of desorption temperature of pyridine-titrated AM; (d) plots of  $2\ln T_m - \ln \beta$  vs  $1/T_m$  for the AM and  $x\text{Sn-AM}$  samples.

( $S_{\text{MA}}$ ), and byproducts as a function of time on stream, is shown in Fig. S12 (Appendix A). After an induction period of 1.5 h, the  $X_{\text{DME}}$  reaches the maximum and then decreases gradually in the following 7 h for all catalysts. The initial catalytic results at 1.5 h are displayed in Fig. 7. As anticipated, stronger BAS in the 8-MRs result in an improved reactivity in DME carbonylation. To illustrate the effect of different Sn species, the performances of HM, AM, and Sn-modified MOR prepared by different methods were compared (Fig. 7(a)). The high MA selectivity (>99.4%) is due to the steric confinement of the 8-MR channels [55,56]. The highest  $\text{STY}_{\text{MA}}$  (431  $\text{g}\cdot\text{kg}^{-1}\cdot\text{h}^{-1}$ ) was achieved over 0.17Sn-AM, because of its strongest acidity. In contrast, the other four catalysts show similar MA yields. It should be noted that the Sn contents in these samples are identical. Thus, the results suggest that mild alkaline treatment and  $\text{SnO}_2$  species have a negligible effect on the catalytic performance, and that framework defects are a prerequisite to form open Sn sites.

To further demonstrate the contribution of the open Sn sites, we tested MORs with different Sn loadings.  $\text{STY}_{\text{MA}}$  exhibits a volcanic trend and achieves the maximum at 0.17Sn-AM by increasing the Sn content from 0 to 0.28% (Fig. 7(b)). The calculated TOFs based specifically on the  $B_{8\text{-MR}}$  reflect the intrinsic activity of the active sites. The TOF is improved with increased Sn incorporation, as shown in Fig. 8, in which the  $\ln$  TOF is plotted as a function of

the acidic strength (i.e.,  $E_{\text{des}}$ ). The linear correlation provides a solid piece of evidence that the enhanced acidic strength in the 8-MRs resulting from open Sn sites contributes to the improved activity in DME carbonylation.

### 3.5. Insight into the promoting mechanism of the Sn-modified MOR

The mechanism of DME carbonylation on H-MOR has been well documented by both experimental and theoretical studies. Possible intermediates and transient states have been proposed based on *in situ* IR, NMR, isotopic tracing, and DFT calculations [15,56–60]. In general, it is accepted that the process includes three main stages: DME dissociative adsorption to form methyl groups, acetyl formation through CO insertion, and MA formation through the surface reaction between the acetyl group and another DME. *In situ* IR is a powerful technique to detect key intermediates (e.g., methyl, acetyl) as well as adsorbed species (e.g., methanol, MA) and has been commonly used to investigate the mechanism of DME carbonylation. If the open Sn sites function as a synergetic site for catalyzing the reaction, new chemical bonds or intermediates should be formed, evidenced by band shifts or new peaks in spectroscopic measurements. Therefore, we performed DME-CO-DME sequent adsorption in an *in situ* IR cell and compared the spectra obtained over AM and 0.17Sn-AM. As shown in Fig. S13 (Appendix A), at the three stages, the IR spectra of AM and 0.17Sn-AM are almost identical. As neither a new peak nor a band shift was observed over the Sn-modified sample, we speculate that the Sn open sites do not directly take part in the reaction. In other words, the elementary steps of DME carbonylation over 0.17Sn-AM are the same as those of pure H-MOR.

However, an interesting finding from the kinetic studies is that the apparent activation energies ( $E_{\text{app}}$ ) of HM and AM are almost identical (i.e., 86 and 87  $\text{kJ}\cdot\text{mol}^{-1}$ ), while that of 0.17Sn-AM decreases to 79  $\text{kJ}\cdot\text{mol}^{-1}$  (Fig. 9), shedding some light on the origin

**Table 4**

$E_{\text{des}}$  of  $\text{NH}_3$  and intensities of the peak at  $2316\text{ cm}^{-1}$  in the  $\text{CD}_3\text{CN}$ -adsorption IR spectra.

Sample	$E_{\text{des}}$ ( $\text{kJ}\cdot\text{mol}^{-1}$ )	Intensity (a.u.)
AM	105	0
0.1Sn-AM	115	0.097
0.17Sn-AM	124	0.163
0.28Sn-AM	121	0.128

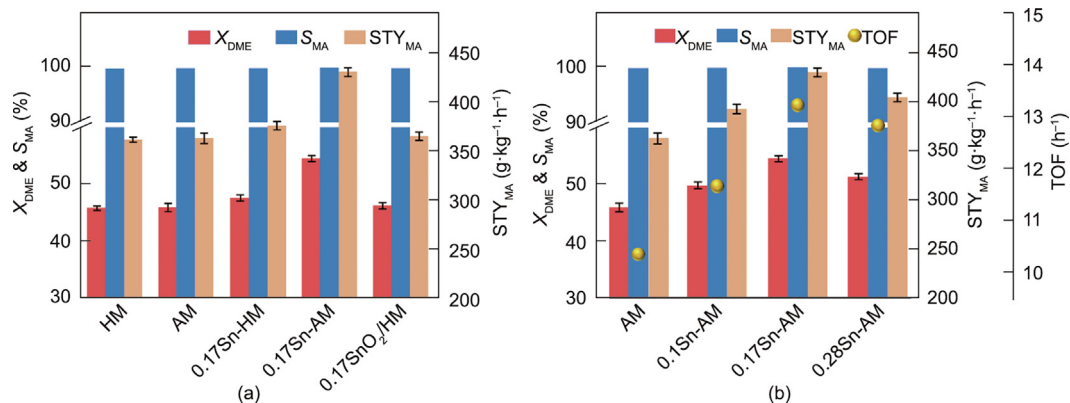


**Fig. 7.** (a)  $X_{DME}$ ,  $S_{MA}$ , and  $STY_{MA}$  of DME carbonylation over the HM, AM, and Sn-MOR catalysts prepared via different methods. (b)  $X_{DME}$ ,  $S_{MA}$ ,  $STY_{MA}$ , and TOF of DME carbonylation over AM and xSn-AM. Reaction conditions: 200 °C, 1.5 MPa,  $V_{DME}:V_{CO} = 1:49$ , GHSV = 6000 h<sup>-1</sup>.

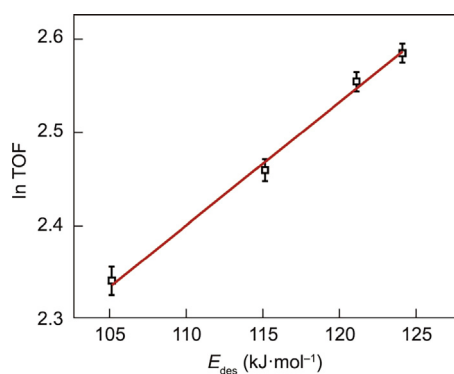


**Fig. 8.** Correlation of ln TOF with  $E_{des}$  over the AM, 0.1Sn-AM, 0.17Sn-AM, and 0.28Sn-AM catalysts.

of the improved catalytic activity. Therefore, we attempted to interpret the decreased activation energy after Sn modification by means of a combined experimental and DFT study. All DFT calculations were performed on the H-[Al,Sn]-MOR model with Sn sitting at the T3-LR site, considering that the BAS at T3-O33 has the strongest acidity in comparison with the models with other Sn locations. The energy profile diagrams for the elementary steps are shown in Fig. 10. The optimized structures of the reactants and intermediates, as well as the transition states, are shown in Figs. S14 and S15 in Appendix A.

At the beginning of the reaction, DME adsorbs on the BAS, forming the protonated DME. The adsorption energies of this process are  $-92$  kJ·mol<sup>-1</sup> for H-[Al]-MOR and  $-125$  kJ·mol<sup>-1</sup> for H-[Al,

Sn]-MOR, indicating that stronger acidity stabilizes DME adsorption. The activation barrier of DME dissociation is  $72$  kJ·mol<sup>-1</sup> on H-[Al,Sn]-MOR, which is lower than that on H-[Al]-MOR ( $95$  kJ·mol<sup>-1</sup>). This result indicates that DME dissociation occurs much faster over Sn-MOR. Fig. 11(a) shows the MS signals of DME and CH<sub>3</sub>OH after exposing the catalysts to DME. It is clear that the formation rate of CH<sub>3</sub>OH over 0.17Sn-AM is accelerated because of its stronger acidity, which agrees well with the above DFT calculations. This conclusion is also in line with our previous observations in heteropolyacids with different strength of BAS [21,22]. The next step is the formation of acetyl via CO insertion into the methyl. As shown in Fig. 10, the energy barriers are  $101$  kJ·mol<sup>-1</sup> for H-[Al]-MOR and  $90$  kJ·mol<sup>-1</sup> for H-[Al,Sn]-MOR, suggesting that the formation of acetyl on Sn-modified MOR is significantly faster than that on MOR. The formation rate of acetyl over HM and 0.17Sn-AM was compared using the characteristic feature of acetyl ( $1637$  cm<sup>-1</sup>, C=O) in the IR spectra (Fig. S16 in Appendix A). Fig. 11(b) presents the normalized intensity of the band at  $1637$  cm<sup>-1</sup> over time; it can be seen that the formation rate of acetyl over 0.17Sn-AM is faster than that over HM, which is consistent with the DFT results. Finally, MA is generated through the interaction between the acetyl intermediate and gaseous DME. The corresponding activation barriers over the two samples are almost identical (Fig. 10; i.e.,  $115$  and  $113$  kJ·mol<sup>-1</sup>), suggesting that the formation of MA is not significantly affected by the acidic strength. Once DME is introduced to the acetyl-saturated zeolites, the MA signals on HM and 0.17Sn-AM show the same trend (Fig. 11 (c)). This finding supports the above DFT calculation results. The gradual and slight decrease of the DME signal after 20–30 min is probably due to the participation of DME in coke formation.

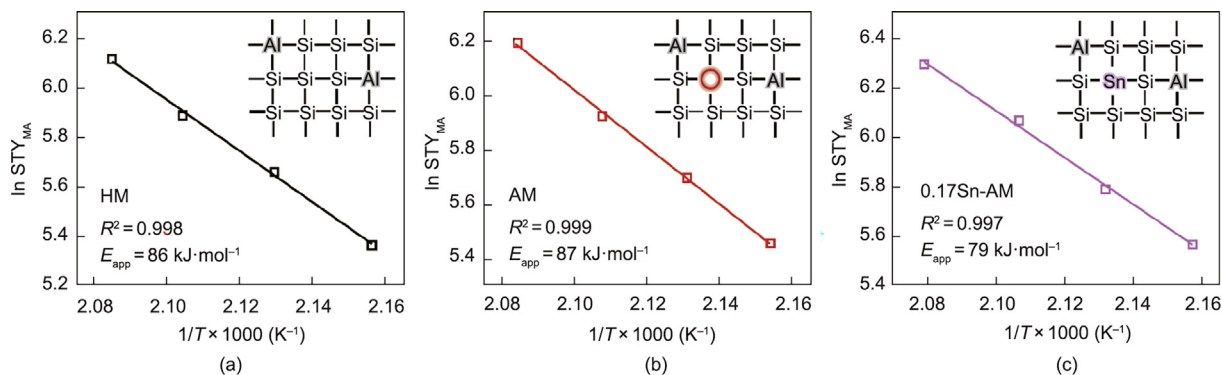


**Fig. 9.** Arrhenius plots of DME carbonylation over (a) HM, (b) AM, and (c) 0.17Sn-AM.

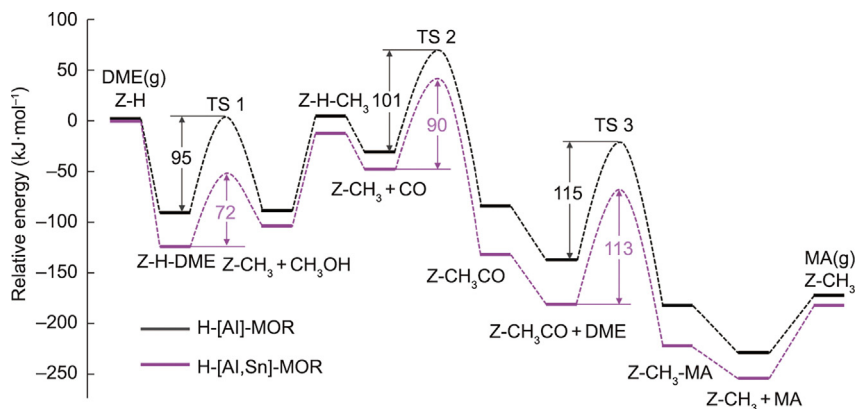


Fig. 10. Energy profile diagrams for the elementary steps. TS: transition state.

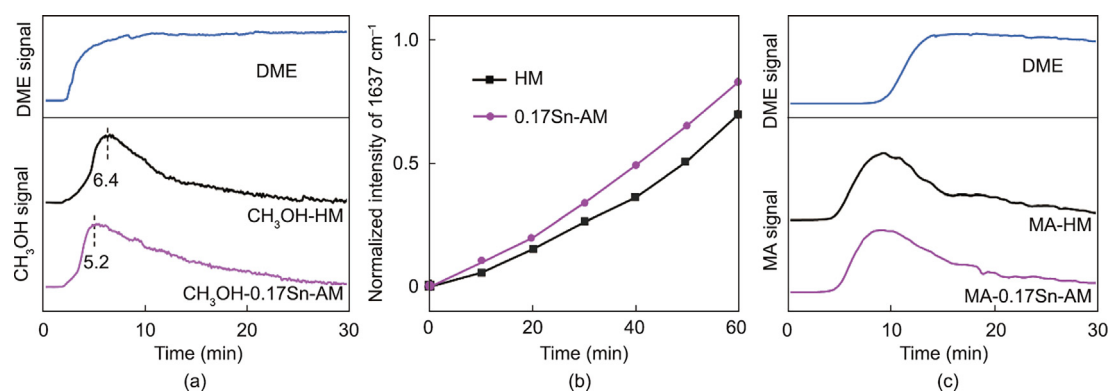


Fig. 11. (a) MS signals of  $\text{CH}_3\text{OH}$  during DME dissociation; (b) normalized intensity of the band at  $1637\text{ cm}^{-1}$  (C=O vibration in acetyl) in IR spectra when CO is exposed to the  $\text{CH}_3$ -saturated zeolite; (c) MS signal of MA during the interaction between DME and acetyl-saturated zeolite.

## 4. Conclusions

In summary, a series of Sn-modified zeolites with enhanced acidity in 8-MR channels were designed and successfully synthesized. A theoretical DFT study suggested that tetrahedral coordinated open Sn sites would exhibit a pronounced enhancement in acidic strength. To fabricate the Sn-modified MOR as predicted, a two-step post-synthetic strategy consisting of the removal of framework Si and the incorporation of Sn into the generated vacant T sites was proposed for the first time. A comprehensive characterization program confirmed that isolated tetrahedral Sn species in an open configuration were successfully engineered and that framework defects are a prerequisite for Sn incorporation. The  $E_{\text{des}}$  obtained from  $\text{NH}_3$ -IR-TPD demonstrated that the BAS in 8-MR channels were strengthened after Sn introduction, in accordance with the results of  $^{13}\text{C}$  CP/MAS NMR spectra. Moreover, as the amount of open Sn sites increased, the acidity became stronger. As a result, an improved catalytic performance was achieved on the Sn-modified MOR catalysts. Kinetic studies together with further DFT calculations revealed that the enhanced acidity of the BAS in the 8-MRs stabilizes DME adsorption and accelerates DME dissociation and acetyl formation. The results demonstrate the feasibility of engineering heteroatom-modified zeolite by creating Si defects while retaining the Brønsted acidity. This mechanistic understanding and promising strategy that precisely modulates the acidic strength of zeolites will contribute to the development of zeolite catalysts for Brønsted acid-catalyzed reactions.

## Acknowledgments

We greatly acknowledge the National Natural Science Foundation of China (21978209 and 22008177) and the Royal Society International Collaboration Award (ICA\R1\180317).

## Compliance with ethics guidelines

Ying Li, Man Yu, Guodong Qi, Yunduo Liu, Jing Lv, Shouying Huang, and Xinbin Ma declare that they have no conflict of interest or financial conflicts to disclose.

## Appendix A. Supplementary data

Supplementary data to this article can be found online at <https://doi.org/10.1016/j.eng.2023.01.020>.

## References

- [1] Yang L, Wang C, Zhang L, Dai W, Chu Y, Xu J, et al. Stabilizing the framework of SAPO-34 zeolite toward long-term methanol-to-olefins conversion. *Nat Commun* 2021;12:4661–71.
- [2] Del Campo P, Navarro MT, Shaikh SK, Khokhar MD, Aljumah F, Martinez C, et al. Propene production by butene cracking. Descriptors for zeolite catalysts. *ACS Catal* 2020;10(20):11878–91.
- [3] Liu S, He Y, Zhang H, Chen Z, Lv E, Ren J, et al. Design and synthesis of Ga-doped ZSM-22 zeolites as highly selective and stable catalysts for *n*-dodecane isomerization. *Catal Sci Technol* 2019;9(11):2812–27.

- [4] Liu Y, Barath E, Shi H, Hu J, Camaioni DM, Lercher JA. Solvent-determined mechanistic pathways in zeolite-H-BEA-catalysed phenol alkylation. *Nat Catal* 2018;1(2):141–7.
- [5] Li Y, Yu J. Emerging applications of zeolites in catalysis, separation and host-guest assembly. *Nat Rev Mater* 2021;6(12):1156–74.
- [6] Jones AJ, Iglesia E. The strength of brønsted acid sites in microporous aluminosilicates. *ACS Catal* 2015;5(10):5741–55.
- [7] Arvidsson AA, Plessow PN, Studt F, Hellman A. Influence of acidity on the methanol-to-DME reaction in zeotypes: a first principles-based microkinetic study. *J Phys Chem C* 2020;124(27):14658–63.
- [8] Jones AJ, Carr RT, Zones SI, Iglesia E. Acid strength and solvation in catalysis by MFI zeolites and effects of the identity, concentration and location of framework heteroatoms. *J Catal* 2014;312:58–68.
- [9] Shi Z, Neurock M, Bhan A. Methanol-to-olefins catalysis on HSSZ-13 and HSAPO-34 and its relationship to acid strength. *ACS Catal* 2021;11(3):1222–32.
- [10] Yang D, Sararuk C, Wang H, Zhang SJ, Li ZX, Li CS. Effect of metal ion in bulk VPO in aldol condensation of formaldehyde and methyl acetate to methyl acrylate. *Ind Eng Chem Res* 2018;57(1):93–100.
- [11] Wang BH, Ge BM, Zhu J, Wang LN. Process optimization study on the carbonylation of methyl acetate. *Chin J Chem Eng* 2018;26(9):1937–42.
- [12] Dunás P, Murfin LC, Nilsson OJ, Jame N, Lewis SE, Kann N. Azulene functionalization by iron-mediated addition to a cyclohexadiene scaffold. *J Org Chem* 2020;85(21):13453–65.
- [13] Portilho Trentini C, de Mello BTF, Ferreira Cabral V, da Silva C. Crambe seed oil: extraction and reaction with dimethyl carbonate under pressurized conditions. *J Supercrit Fluids* 2020;159:104780.
- [14] Zhou W, Kang J, Cheng K, He S, Shi J, Zhou C, et al. Direct conversion of syngas into methyl acetate, ethanol, and ethylene by relay catalysis via the intermediate dimethyl ether. *Angew Chem Int Ed* 2018;57(37):12012–6.
- [15] Boronat M, Martínez-Sánchez C, Law D, Corma A. Enzyme-like specificity in zeolites: a unique site position in mordenite for selective carbonylation of methanol and dimethyl ether with CO. *J Am Chem Soc* 2008;130(48):16316–23.
- [16] Bhan A, Allian AD, Sunley GJ, Law DJ, Iglesia E. Specificity of sites within eight-membered ring zeolite channels for carbonylation of methyls to acetals. *J Am Chem Soc* 2007;129(16):4919–24.
- [17] Ham H, Jung HS, Kim HS, Kim J, Cho SJ, Lee WB, et al. Gas-phase carbonylation of dimethyl ether on the stable seed-derived ferrierite. *ACS Catal* 2020;10(9):5135–46.
- [18] Lusardi M, Chen TT, Kale M, Kang JH, Neurock M, Davis ME. Carbonylation of dimethyl ether to methyl acetate over SSZ-13. *ACS Catal* 2020;10(1):842–51.
- [19] Feng X, Yao J, Li H, Fang Y, Yoneyama Y, Yang G, et al. A brand new zeolite catalyst for carbonylation reaction. *Chem Commun* 2019;55(8):1048–51.
- [20] Xiong Z, Zhan E, Li M, Shen W. DME carbonylation over a HSUZ-4 zeolite. *Chem Commun* 2020;56(23):3401–4344.
- [21] Shen HB, Li Y, Huang SY, Cai K, Cheng ZZ, Lv J, et al. The carbonylation of dimethyl ether catalyzed by supported heteropoly acids: the role of Brønsted acid properties. *Catal Today* 2019;330:117–23.
- [22] Cai K, Li Y, Shen H, Cheng Z, Huang S, Wang Y, et al. A density functional theory study on the mechanism of dimethyl ether carbonylation over heteropolyacids catalyst. *Front Chem Sci Eng* 2021;15(2):319–29.
- [23] Cai K, Huang S, Li Y, Cheng Z, Lv J, Ma X. Influence of acid strength on the reactivity of dimethyl ether carbonylation over H-MOR. *ACS Sustain Chem Eng* 2019;7(2):2027–34.
- [24] Verboekend D, Milina M, Perez-Ramirez J. Hierarchical silicoaluminophosphates by postsynthetic modification: influence of topology, composition, and silicon distribution. *Chem Mater* 2014;26(15):4552–62.
- [25] Machado V, Rocha J, Carvalho AP, Martins A. Modification of MCM-22 zeolite through sequential post-synthesis treatments. Implications on the acidic and catalytic behaviour. *Appl Catal A* 2012;445–446:329–38.
- [26] Gao P, Wang Q, Xu J, Qi G, Wang C, Zhou X, et al. Brønsted/Lewis acid synergy in methanol-to-aromatics conversion on Ga-modified ZSM-5 zeolites, as studied by solid-state NMR spectroscopy. *ACS Catal* 2018;8(1):69–74.
- [27] Yu Z, Li S, Wang Q, Zheng A, Jun X, Chen L, et al. Brønsted/Lewis acid synergy in H-ZSM-5 and H-MOR zeolites studied by <sup>1</sup>H and <sup>27</sup>Al DQ-MAS solid-state NMR spectroscopy. *J Phys Chem C* 2011;115(45):22320–7.
- [28] Li S, Zheng A, Su Y, Zhang H, Chen L, Yang J, et al. Brønsted/Lewis acid synergy in dealuminated HY zeolite: a combined solid-state NMR and theoretical calculation study. *J Am Chem Soc* 2007;129(36):11161–71.
- [29] Cho HJ, Dornath P, Fan W. Synthesis of hierarchical Sn-MFI as Lewis acid catalysts for isomerization of cellulose sugars. *ACS Catal* 2014;4(6):2029–37.
- [30] Tang B, Dai W, Wu C, Guan N, Li L, Hunger M. Improved postsynthesis strategy to Sn-beta zeolites as Lewis acid catalysts for the ring-opening hydration of epoxides. *ACS Catal* 2014;4(8):2801–10.
- [31] Injongkol Y, Maihom T, Treesukul P, Sirijaraensre J, Boekfa B, Limtrakul J. Theoretical study on the reaction mechanism of hydrogenation of furfural to furfuryl alcohol on Lewis acidic BEA zeolites: effects of defect structure and tetraavalent metals substitution. *Phys Chem Chem Phys* 2017;19(35):24042–8.
- [32] Li Y, Huang S, Cheng Z, Cai K, Li L, Milan E, et al. Promoting the activity of Ce-incorporated MOR in dimethyl ether carbonylation through tailoring the distribution of brønsted acids. *Appl Catal B* 2019;256:117777.
- [33] Bates JS, Bukowski BC, Harris JW, Greeley J, Gounder R. Distinct catalytic reactivity of Sn substituted in framework locations and at defect grain boundaries in Sn-zeolites. *ACS Catal* 2019;9(7):6146–68.
- [34] Harris JW, Cordon MJ, Di Iorio JR, Vega-Vila JC, Ribeiro FH, Gounder R. Titration and quantification of open and closed Lewis acid sites in Sn-beta zeolites that catalyze glucose isomerization. *J Catal* 2016;335:141–54.
- [35] Qi L, Zhang Y, Conrad MA, Russell CK, Miller J, Bell AT. Ethanol conversion to butadiene over isolated zinc and yttrium sites grafted onto dealuminated beta zeolite. *J Am Chem Soc* 2020;142(34):14674–87.
- [36] Antunes MM, Lima S, Neves P, Magalhães AL, Fazio E, Fernandes A, et al. One-pot conversion of furfural to useful bio-products in the presence of a Sn, Al-containing zeolite beta catalyst prepared via post-synthesis routes. *J Catal* 2015;329:522–37.
- [37] Petranovskii V, Gurin V, Machorro R. Spectroscopic observation and *ab initio* simulation of copper clusters in zeolites. *Catal Today* 2005;107–108:892–900.
- [38] Dijkmans J, Dusselier M, Gabriels D, Houthoofd K, Magusin PCMM, Huang S, et al. Cooperative catalysis for multistep biomass conversion with Sn/Al beta zeolite. *ACS Catal* 2015;5(2):928–40.
- [39] Paris C, Moliner M, Corma A. Metal-containing zeolites as efficient catalysts for the transformation of highly valuable chiral biomass-derived products. *Green Chem* 2013;15(8):2101–9.
- [40] Dai W, Wang C, Tang B, Wu G, Guan N, Xie Z, et al. Lewis acid catalysis confined in zeolite cages as a strategy for sustainable heterogeneous hydration of epoxides. *ACS Catal* 2016;6(5):2955–64.
- [41] Yuan E, Dai W, Wu G, Guan N, Hunger M, Li L. Facile synthesis of Sn-containing MFI zeolites as versatile solid acid catalysts. *Microporous Mesoporous Mater* 2018;270:265–73.
- [42] Campelo JM, Luna D, Luque R, Marinas JM, Romero AA, Calvino JJ, et al. Synthesis of acidic Al-MCM-48: influence of the Si/Al ratio, degree of the surfactant hydroxyl exchange, and post-treatment in NH<sub>4</sub>F solution. *J Catal* 2005;230(2):327–38.
- [43] Yang X, Liu Y, Li X, Ren J, Zhou L, Lu T, et al. Synthesis of Sn-containing nanosized beta zeolite as efficient catalyst for transformation of glucose to methyl lactate. *ACS Sustain Chem Eng* 2018;6(7):8256–65.
- [44] Anquetil R, Saussey J, Lavalley JC. Confinement effect on the interaction of hydroxy groups contained in the side pockets of H-mordenite with nitriles; a FT-IR study. *Phys Chem Chem Phys* 1999;1(4):555–60.
- [45] Daniell W, Topsoe NY, Knozinger H. An FTIR study of the surface acidity of USY zeolites: comparison of CO, CD<sub>3</sub>CN, and C<sub>5</sub>H<sub>5</sub>N probe molecules. *Langmuir* 2001;17(20):6233–9.
- [46] Otomo R, Kosugi R, Kamiya Y, Tatsumi T, Yokoi T. Modification of Sn-beta zeolite: characterization of acidic/basic properties and catalytic performance in Baeyer-Villiger oxidation. *Catal Sci Technol* 2016;6(8):2787–95.
- [47] Qi G, Wang Q, Xu J, Wu Q, Wang C, Zhao X, et al. Direct observation of tin sites and their reversible interconversion in zeolites by solid-state NMR spectroscopy. *Commun Chem* 2018;1(1):22.
- [48] Yakimov AV, Kolyagin YG, Tolborg S, Vennestrøm PNR, Ivanova II. <sup>119</sup>Sn MAS NMR study of the interaction of probe molecules with Sn-BEA: the origin of penta- and hexacoordinated tin formation. *J Phys Chem C* 2016;120(49):28083–92.
- [49] Wang M, Huang S, Lu J, Cheng Z, Li Y, Wang S, et al. Modifying the acidity of H-MOR and its catalytic carbonylation of dimethyl ether. *Chin J Catal* 2016;37(9):1530–7.
- [50] Emeis CA. Determination of integrated molar extinction coefficients for infrared absorption bands of pyridine adsorbed on solid acid catalysts. *J Catal* 1993;141(2):347–54.
- [51] Xu J, Zheng A, Wang X, Qi G, Su J, Du J, et al. Room temperature activation of methane over Zn modified H-ZSM-5 zeolites: insight from solid-state NMR and theoretical calculations. *Chem Sci* 2012;3(10):2932–40.
- [52] Barich DH, Nicholas JB, Xu T, Haw JF. Theoretical and experimental study of the <sup>13</sup>C chemical shift tensors of acetone complexed with Brønsted and Lewis acids. *J Am Chem Soc* 1998;120(47):12342–50.
- [53] Li S, Huang SJ, Shen W, Zhang H, Fang H, Zheng A, et al. Probing the spatial proximities among acid sites in dealuminated H-Y zeolite by solid-state NMR spectroscopy. *J Phys Chem C* 2008;112(37):14486–94.
- [54] Ono LK, Roldan CB. Size effects on the desorption of O<sub>2</sub> from Au<sub>2</sub>O<sub>3</sub>/Au<sup>0</sup> nanoparticles supported on SiO<sub>2</sub>: a TPD study. *J Phys Chem C* 2008;112(47):18543–50.
- [55] Cao K, Fan D, Li L, Fan B, Wang L, Zhu D, et al. Insights into the pyridine-modified MOR zeolite catalysts for DME carbonylation. *ACS Catal* 2020;10(5):3372–80.
- [56] Cheung P, Bhan A, Sunley GJ, Law DJ, Iglesia E. Site requirements and elementary steps in dimethyl ether carbonylation catalyzed by acidic zeolites. *J Catal* 2007;245(1):110–23.
- [57] Li BJ, Xu J, Han B, Wang XM, Qi GD, Zhang ZF, et al. Insight into dimethyl ether carbonylation reaction over mordenite zeolite from *in-situ* solid-state NMR spectroscopy. *J Phys Chem C* 2013;117(11):5840–7.
- [58] Rasmussen DB, Christensen JM, Temel B, Studt F, Moses PG, Rossmelil J, et al. Ketene as a reaction intermediate in the carbonylation of dimethyl ether to methyl acetate over mordenite. *Angew Chem Int Ed* 2015;54(25):7261–4.
- [59] Zhou H, Zhu WL, Shi L, Liu HC, Liu SP, Ni YM, et al. *In situ* DRIFT study of dimethyl ether carbonylation to methyl acetate on H-mordenite. *J Mol Catal Chem* 2016;417:1–9.
- [60] Li Y, Huang SY, Cheng ZZ, Wang SP, Ge QF, Ma XB. Synergy between Cu and Brønsted acid sites in carbonylation of dimethyl ether over Cu/H-MOR. *J Catal* 2018;365:440–9.